

ORIGINAL ARTICLE

Signal deformation fault monitors for dual-frequency GBAS

Junesol Song | Carl Milner  | Ikhlas Selmi

ENAC, Université de Toulouse, Toulouse, France

Correspondence

Carl Milner, ENAC, Université de Toulouse, 7 Avenue Edouard Belin, 31400 Toulouse, France.
Email: milner@recherche.enac.fr

Funding information

Single European Sky ATM Research (SESAR), Grant/Award Number: SESAR 2020 PJ14-03-01 WP8 T04

Abstract

This paper proposes a new dual-frequency signal deformation fault monitor, which can effectively reduce the time delay at the Ground-Based Augmentation System (GBAS) airborne user from the airborne filter initialization to the time when it incorporates ground corrections and user measurements for navigation, assuring the system integrity at the same time. The new monitor is applied together with the existing Honeywell signal deformation monitor and Code-Carrier Divergence monitors to protect the airborne users against the signal deformation faults. In addition, the probability of missed detection of the monitors is assessed for the GBAS Approach Service Types (GAST) F, which supports the Category (CAT) II and III precision approaches based on the multifrequency and multiconstellation. As a result, the proposed monitor together with the Honeywell and the CCD monitors is able to assure the system integrity for all fault cases within the threat space. The result also shows that the addition of the proposed monitor can reduce the time delay by 80%; moreover, it can even reduce the recommended time delay below 50 s. Consequently, it can avoid the unnecessary delays for the use of newly available satellites at the airborne.

1 | INTRODUCTION

The Ground-Based Augmentation System (GBAS) has been developed to provide corrections and integrity data in the proximity of airports operating precision approach. The GBAS Approach Service Type (GAST) C, which supports the Category (CAT) I precision approach with a 200 ft decision height, was standardized by the International Civil Aviation Organization (ICAO) in previous study.¹ Recently, GAST D supporting the CAT II and III precision approaches with a decision height down to 50 ft has also been standardized at the international level.² One of the most significant differences between GAST C and GAST D is the requirement on the ranging source fault monitors. It is mandatory to have those monitors to protect airborne users of GBAS against satellite-related faults, such as signal deformation, code/carrier divergence, excessive pseudorange acceleration, and erroneous broadcast of ephemeris data.^{1–3} These monitors should

ensure the system integrity even under such a fault.⁴ The findings from former research on CAT I are based on a requirements methodology known as the Instrument Landing System (ILS) look-alike concept. However, this approach was found to be too conservative and therefore limiting for CAT II/III.⁵ Consequently, the requirements on the Probability of Missed Detection (PMD) of the monitors for GAST D have been derived based on a different methodology.³ The first contribution of this paper is then to present in the public domain a scheme for meeting the GAST D ranging source monitoring requirements for the signal deformation threat in order to validate that such a requirement can be met.

In future iterations of GBAS, the proposal is to utilize additional modernized signals, such as the GPS L5 and Galileo E1c/E5a signals, which should improve navigation accuracy and integrity performance. This dual-frequency solution applied to CAT II/III operations is designated as GAST F. The same requirement on the

PMD of the ranging source fault monitors may be applied to GAST F subject to caveats regarding the processing mode, as discussed later in the paper.

Signal deformation fault monitors must detect satellite signal distortions to prevent user receivers from experiencing misleading information (MI) in the high-integrity augmentation systems of GBAS and the Satellite-Based Augmentation System (SBAS). These distortions have occurred on the GPS L1 C/A code, which results from a malfunction of the analog or digital signal generating hardware onboard the satellite^{6,7} and could potentially reoccur in the future in spite of improved satellite design. Consequently, under failure, the correlation function is distorted, which leads to an incorrectly estimated code delay and a bias-like error being included in the pseudorange measurement. Moreover, this bias error can vary according to receiver tracking configurations in terms of chip spacing, precorrelation filter type, and its bandwidth. To protect ground and user receivers against this type of range fault after-the-fact, it is mandatory to have monitors to detect and remove those distorted signals. It is clear that the most effective way to have these monitors onboard for detecting the faults is at the incipient stage. However, because it is not possible currently, the proposed monitor in this paper is for the operation at the GBAS ground station.

In the work undertaken, there are two key contributions. One is to design the new dual-frequency monitors as well as the definition of a combination of monitors to protect against signal deformations. Three types of monitors are used to detect signal deformations in this study: the first is the signal deformation monitor developed by Honeywell in 2006,⁸ the second is a variation of the Code-Carrier Divergence (CCD) monitor developed by Ecole Nationale de l'Aviation Civile (ENAC),⁹ and the third is a novel Divergence-Free (DF) innovation monitor. This novel DF-innovation monitor, which was originally introduced in an earlier version of this paper,¹⁰ compares a dummy DF pseudorange to the predicted DF pseudorange at the current epoch, which is propagated from the previous epoch using the innovation of the carrier phase. Accordingly, the novel monitor is sensitive to capturing step faults in the pseudorange measurements, yet is not impacted by ionospheric delay which reduces the efficiency of existing step detectors. In addition, the time constant of the smoothing filter for the DF pseudorange measurements has been determined based on the analysis on the temporal correlation of the DF measurements.

The other contribution is the assessment of GBAS signal deformation fault monitors under the proposed GAST F solution. For the assessment, the threat model for the GPS L1 C/A signal is adopted from the one defined in the

ICAO standards.¹ Agreement on the threat space of the modernized signals has not yet been reached at the standardization level. However, research has proposed threat spaces for those signals, taking into account different modulation, chipping rates, and correlation functions.¹¹ Among them, the threat spaces for Galileo signals are under the validation process prior to standardization. These definitions are adopted as the threat spaces for the modernized signals in this paper. Based on these threat models, signal deformation fault monitors are tested for single- and dual-frequency modes, which represent GAST D and F, respectively. To be more specific, dual-frequency signal deformation fault monitors for GPS L1/L5 and Galileo E1c/E5a are tested under dual-frequency navigation modes, such as Ionosphere-Free (IF) smoothing, whether they comply with the PMD requirement according to the differential range errors. This study assumed that only a single frequency may be faulted at one time according to the general consensus.¹² Simulations have then been performed to investigate the monitoring performance and check under what conditions compliance with the requirement is achieved.

This paper is organized as follows. First, the proposed DF-innovation monitor will be introduced, and the time constant of the smoothing filter for the DF pseudorange combination will be determined taking into account the temporal correlation of the measurements. Second, the simulation environment, including the threat space of the faults for GPS and Galileo signals, receiver configurations, and fault onset scenario, will be presented. The nominal and the deformed GNSS code sequences are generated to compute the correlator outputs and correspond bias errors according to the values given by the threat model parameters and receiver configurations. The multi-correlator outputs are used to compute the Honeywell monitor test statistics and the bias errors are added to the simulated pseudorange measurements, which are used for computing the CCD and DF-innovation monitors as well as the differential range error. Third, the PMD of the monitors according to the differential range error is used to determine the compliance with respect to the requirement defined in the standards. Finally, the conclusions will follow.

2 | RELATED WORK

For the given GPS L1 C/A threat space of the signal deformation fault, the performance of the signal deformation fault monitors has been assessed with respect to the requirements of the different levels of precision approach. Phelts⁷ proposed the Signal Quality Monitor (SQM) using multicorrelator outputs to detect the signal deformation

faults and validated that the proposed monitors can effectively protect airborne users for CAT I landings. In his approach, the maximum differential pseudorange error associated with the signal deformation fault is compared with the Maximum Error Range Residuals (MERR), which is derived based on the assumption of the worst-case satellite geometry.¹³ Zaugg¹⁴ later proposed an integrity approach that takes into account the relation between the maximum allowable error, the probability of missed detection, and the probability of the misleading information thoroughly. Rife and Phelts¹⁵ further improved this approach by considering the transient phase before the carrier smoothing filter reaches steady-state, proposing the time-varying MERR. The Honeywell signal deformation fault monitor has been proposed, and its integrity performance has been proven for GAST C.⁸ In addition, the performance of the same monitor, together with the CCD monitor and the step detector for the detection of the signal deformation fault, has been validated for the GAST D using the GPS L1 C/A signal, which uses the minimum PMD among the three monitors.⁵ It concludes that for airborne delays of 25 s before incorporating a filtered measurement, the PMD of the monitors was compliant for all fault cases and receiver configurations. For GAST F, using multiconstellation and multifrequency signals, the assessment of the monitor has not been conducted thoroughly. Work has been done by Thales in 2015 on the assessment of the three types of monitors for the signal deformation faults¹⁶; however, the monitors used for the test and the threat space for GPS L5 and Galileo signals were not presented within the public domain.

3 | MONITORS FOR SIGNAL DEFORMATION FAULTS

In this study, three types of monitors are used for detecting signal deformation faults: the Honeywell signal deformation monitor,⁸ the ENAC DF CCD monitor,⁹ and the proposed DF-innovation monitor. The Honeywell signal deformation monitor and ENAC CCD monitors have been proposed, and their performance has been fully or partially validated; they are not described in detail in this paper. The Honeywell signal deformation monitor has been validated for the GAST D solution so that it can protect airborne users against Threat Model (TM) types A, B, and C, which have been defined in the ICAO standards for GPS L1 C/A signal,¹ when it is used with the conventional single-frequency CCD monitor and a step detector. Therefore, this study decided to use this monitor as part of detecting signal deformation faults based on multi-correlator outputs. The Honeywell monitor utilizes the

correlator outputs taken from the eight code offset locations ranging from -0.05 to 0.125 chips with a 0.025 -chip interval. Since Galileo E1c signal has the same chipping rate as that of GPS L1 C/A signal, the Honeywell monitor can be used without any modification even if the different modulations are used: Binary Phase Shift Keying (BPSK) for GPS L1 C/A and Composite Binary Offset Carrier (CBOC). However, GPS L5 and Galileo E5a signals, which are modulated as BPSK (10), have a 10 times larger chipping rate; therefore, the code offset ranges for taking correlator outputs and its interval are increased to the factor 10 of the values used for GPS L1 C/A and Galileo E1c signals. That is, the Honeywell monitor uses the correlator outputs at locations ranged from -0.5 to 1.25 chips in this study.

The standard CCD monitor uses the rate of the single-frequency code minus carrier observables filtered by two cascades of a first-order smoothing filter.¹⁷ Based on this, dual-frequency CCD monitors have been proposed and validated for GAST D and F solutions.⁹ Since these monitors have been widely considered for protection against the signal deformation faults,^{5,16} the dual-frequency CCD monitor is also used for the assessment in this study. Conservatively, the minimum PMD among the three monitors is used to assess the PMD compliance at each point in time for the GAST F solution according to the work done by Honeywell and Thales.

3.1 | Measurement model

The pseudorange and carrier phase measurements are defined as

$$\begin{aligned}\rho_j &= r + \iota_j + m_j + \eta_{\rho_j} \\ \varphi_j &= r - \iota_j + N_j + \eta_{\varphi_j} \\ \text{where, } \iota_j &= \gamma \iota_1 \\ \gamma &\equiv \left(\frac{f_1}{f_j} \right)^2,\end{aligned}\tag{1}$$

where

ρ = pseudorange measurement

φ = carrier phase measurement

r = geometry-related term, which includes true geometric range, receiver clock bias, satellite clock bias, and tropospheric delay

ι = ionospheric delay on frequency j (ι_1 : L1 ionospheric delay)

m = multipath error

N = ambiguity error in meter

η = noise error

f = transmit frequency.

The subscript j can have 1 and 5 to indicate L1 and L5 transmit frequencies.

3.2 | Divergence-free innovation monitor

The correlator outputs that are used for the Honeywell monitor are filtered to improve the sensitivity of the monitor to detect the signal deformation faults. In addition, the CCD monitor is also based on the smoothed rate of the Divergence-Free (DF) measurement combinations. Consequently, when the fault occurs, these smoothing filters introduce some response time in the monitor metrics until they reach the steady-state values of the impact of the fault on the monitors. This may limit the performance of the monitors immediately after the fault onset. To deal with this problem, this study proposes the DF-innovation monitor, denoted as q , which measures the difference between the predicted pseudorange and the raw pseudorange error at current epoch, as shown in Equation (2).

$$q_{DFj}(k) \equiv \hat{\rho}_j(k) - \rho_j(k). \quad (2)$$

The symbol k indicates the epoch index and the subscript DF means the DF combination. The predicted pseudorange, $\hat{\rho}_j$, can be computed using the innovation of the carrier phase as in Equation (3).

$$\begin{aligned} \hat{\rho}_j(k) &\equiv \tilde{\rho}_j(k-1) + \Delta\Phi_j(k) \\ \text{where, } \Delta\Phi_j(k) &\equiv \Phi_j(k) - \Phi_j(k-1). \end{aligned} \quad (3)$$

The carrier phase combination for computing the predicted pseudorange is denoted as Φ_j and defined in Equation (4).

$$\begin{aligned} \Phi_1 &\equiv \varphi_1 + 2\frac{\varphi_1 - \varphi_5}{\gamma - 1} = r + \iota_1 + \alpha_1 N_1 + \alpha_2 N_5 + \alpha_1 \eta_{\varphi_1} + \alpha_2 \eta_{\varphi_5} \\ \Phi_5 &\equiv \varphi_5 + 2\gamma\frac{\varphi_1 - \varphi_5}{\gamma - 1} = r + \gamma\iota_1 + \beta_1 N_1 + \beta_2 N_5 + \beta_1 \eta_{\varphi_1} + \beta_2 \eta_{\varphi_5} \\ \text{where, } \alpha_1 &= -\frac{\gamma + 1}{\gamma - 1}, \alpha_2 = \frac{2}{\gamma - 1} \\ \beta_1 &= \frac{-2\gamma}{\gamma - 1}, \beta_2 = \frac{\gamma + 1}{\gamma - 1}. \end{aligned} \quad (4)$$

In Equation (3), the pseudorange with the tilde ($\tilde{\cdot}$) is the filtered value obtained from the divergence-free smoothing filter as shown in Figure 1. For a single-frequency

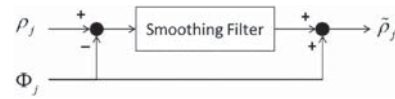


FIGURE 1 Carrier smoothing in dual-frequency modes for the DF-innovation monitor

filter, a pseudorange is also smoothed using carrier phase measurement; however, it suffers from divergence because the ionospheric delays in the pseudorange and carrier phase measurements have opposite signs.¹⁸ This problem can be resolved in the dual-frequency processing, because several measurement combinations, that are free of ionospheric delay, may be defined as inputs to the smoothing filter. The carrier phase measurement combination, Φ_j , defined in Equation (4), is used for computing the DF-innovation monitor in Equation (3) as well as in the smoothing filter shown in Figure 1. This term has the same sign for the ionospheric delay as in the pseudorange measurement, thus it eliminates the code minus the carrier divergence in the smoothing filter. It is assumed that the carrier phase multipath is negligible.

From Equation (2) and Equation (3) and Figure 1, the filtered L1 and L5 pseudoranges can be expressed as the following equation.

$$\begin{aligned} \tilde{\rho}_1 &= r + \iota_1 + \tilde{m}_1 + \tilde{\eta}_{\rho_1} - \alpha_1 \left\{ \tilde{\eta}_{\varphi_1} - \eta_{\varphi_1} \right\} - \alpha_2 \left\{ \tilde{\eta}_{\varphi_5} - \eta_{\varphi_5} \right\} \\ \tilde{\rho}_5 &= r + \gamma\iota_1 + \tilde{m}_5 + \tilde{\eta}_{\rho_5} - \beta_1 \left\{ \tilde{\eta}_{\varphi_1} - \eta_{\varphi_1} \right\} - \beta_2 \left\{ \tilde{\eta}_{\varphi_5} - \eta_{\varphi_5} \right\} \end{aligned} \quad (5)$$

Compared to the raw pseudorange measurements shown in Equation (1), the filtered pseudorange has the smoothed pseudorange multipath and noise error as well as filtered and raw carrier phase noise errors. Finally, the components in the DF-innovation monitor can be expressed as Equation (6).

$$\begin{aligned} q_{DF1}(k) &= \{ \tilde{m}_1(k-1) - m_1(k) \} + \left\{ \tilde{\eta}_{\rho_1}(k-1) - \eta_{\rho_1}(k) \right\} \\ &\quad - \alpha_1 \left\{ \tilde{\eta}_{\varphi_1}(k-1) - \eta_{\varphi_1}(k) \right\} - \alpha_2 \left\{ \tilde{\eta}_{\varphi_5}(k-1) - \eta_{\varphi_5}(k) \right\} \\ q_{DF5}(k) &= \{ \tilde{m}_5(k-1) - m_5(k) \} + \left\{ \tilde{\eta}_{\rho_5}(k-1) - \eta_{\rho_5}(k) \right\} \\ &\quad - \beta_1 \left\{ \tilde{\eta}_{\varphi_1}(k-1) - \eta_{\varphi_1}(k) \right\} - \beta_2 \left\{ \tilde{\eta}_{\varphi_5}(k-1) - \eta_{\varphi_5}(k) \right\} \end{aligned} \quad (6)$$

The DF-innovation monitor is mainly composed of multipath and noise errors. To improve the detection performance of the monitor, the levels of these errors need

to be reduced as much as possible. In Equation (6), the multipath-related error corresponds to the difference between the filtered multipath error at the previous epoch and the raw multipath error at the current epoch. Since the multipath is temporally correlated, the difference depends upon the filter smoothing the time and level of correlation. It is beneficial to employ a small time constant as shown in Figure 1 in order to preserve the correlation between two terms as much as possible. However, for the noise-related terms, it is clear that the noise level will decrease if the time constant of the smoothing filter increases. Since there is a trade-off relationship between reducing multipath and noise related errors, the standard deviations of the DF-innovation monitor are analyzed according to the various time constants of the smoothing filter to design the DF-innovation monitor with the lowest error level using a real data analysis.

3.3 | Determination of the time constant of the smoothing filter for the DF-innovation monitor

Since the multipath error is an environment-dependent term, to avoid obtaining site-, receiver-, or antenna-specific results, the GPS L1 and L5 data were collected from various reference stations equipped with different receiver-antenna pairs as shown in Table 1. Since the

data are collected from research-oriented GBAS reference stations as well as reference stations with various Differential GNSS (DGNSS) and Network Real-Time Kinematic (RTK) applications, we believe that the multipath related environments around the sites are not too severe. The data have been collected with rates of 1 or 2 Hz to compute the standard deviations for various smoothing constants up to 100 s.

To observe the tendency of the smoothing effect according to different time constants, Figure 2 shows the normalized standard deviation according to various time constants with respect to the standard deviation computed for a 100-s time constant for low elevation angles ranging from 5 to 10°. The time constant of the smoothing filter is denoted as τ in the figure. Surprisingly, the error level of the DF-innovation monitor is much smaller when the smaller time constant is used for most of the cases. It can be inferred from this observation that the multipath related error is dominant in the DF-innovation monitor rather than the noise term. For Trimble receivers, the differences in the standard deviation were not prominent according to the time constants unlike other receiver cases for L1 frequency. However, for the L5 frequency, every case exhibits the similar tendencies in terms of the smoothing effect on the standard deviations over the tested time constants. The difference between results from the Trimble and other receivers seems to come from the different characteristics of the

TABLE 1 Reference receivers for the data collection

Reference Stations	Agency	Date	Measurement Interval, Δt , s	Receiver Type	Antenna Type
Tenerife GBAS ground station ^a	Indra navia and Indra satnav within SESAR project	DOY128, 2019 (24 h)	0.5	Novatel Propak6	MLA (ARL-1900)
Barcelona GBAS ground station ^a	Indra navia and Indra satnav within SESAR project	DOY316–317, 2018 (48 h)	0.5	Novatel Propak6	Novatel GNSS-750
YOIN	NGII, South Korea	DOY233, 2019 (24 h)	1	Leica GR50	Leica GNSS Choke Ring
SWIC	Korean Space Weather Center	DOY233, 2019 (24 h)	1	NovAtel GPStation-6	Novatel ANT-C2GA-TW-N
POSG	KIGAM, South Korea	DOY233, 2019 (24 h)	1	Septentrio PolarX5	SEPCHOKE_B2E6 SPKE
NCWR	NGS CORS, USA	DOY169–170, 2019 (48 h)	1	Trimble NetR5	Trimble Zephyr Geodetic Antenna
SUWN	NGII, South Korea	DOY169–170, 2019 (48 h)	1	Trimble NetR9	Trimble GNSS Choke

^aWithin the activity of the Single European Sky ATM Research (SESAR) 2020 PJ14-03-01 WP8 T04.

Abbreviations: DOY, day-of-year; SESAR, Single European Sky ATM Research; MLA, Multipath Limiting Antenna; NGII, National Geographic Information Institute; KIGAM, Korea Institute of Geoscience and Mineral Resources; NGS CORS, National Geodetic Survey Continuously Operating Station.

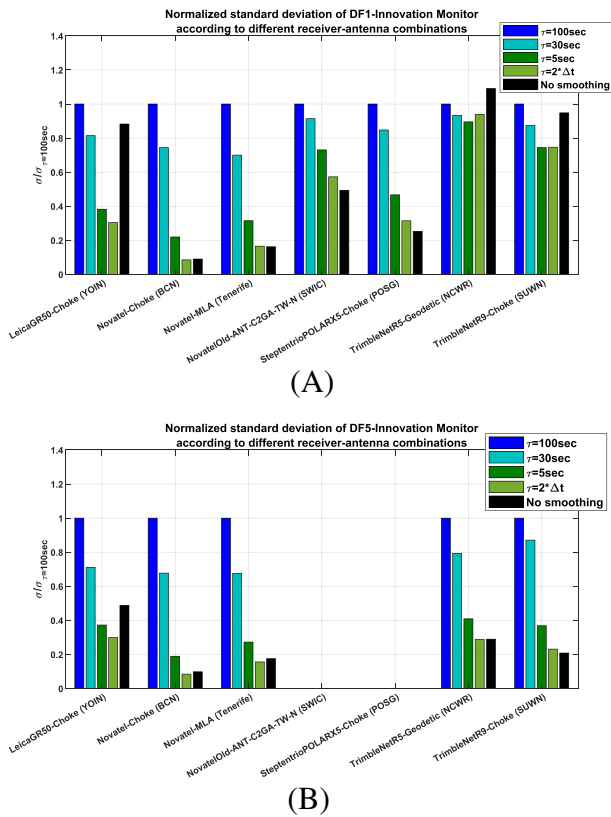


FIGURE 2 Effect of different time constants of smoothing filter on the standard deviation of the DF-innovation monitor computed for elevation angles from 5 to 10° for (A) L1 frequency and (B) L5 frequency (SWIC and POSG were not L5-frequency capable) [Color figure can be viewed at wileyonlinelibrary.com and www.ion.org]

time correlation in the DF-innovation monitor metric. Based on the results shown in Figure 2, the DF-innovation monitor metrics computed using the Trimble measurements seem to have lower time correlations than those computed from other receivers. To verify this argument, the autocorrelations of the monitor metric are

computed. Assuming that the time correlated term, which is mainly due to the multipath error, in the monitor metric can be modeled as a first-order Gauss-Markov process, the time correlation parameter is also computed in Figure 3. Figure 3A depicts the normalized autocorrelations of the DF1-innovation monitor metric for SUWN and POSG reference stations and Tenerife sites. The individual line indicates the normalized autocorrelation function for each measurement arc, and the thick line depicts their median value. It can be clearly observed that the initial slope of the normalized autocorrelation for SUWN, equipped with the Trimble receiver, is much steeper than others for POSG and Tenerife sites. That is, the time constant of the multipath error in the DF-innovation monitor metric is the smallest for the Trimble receiver. Figure 3B shows the median values of the time constants for all receiver sites, and it confirms that the time constant of the multipath error of the DF-innovation monitor metric for L1 frequency is smallest for the sites equipped with Trimble receivers. However, for L5 frequency, the time correlations at those sites are higher than those for L1 frequency, and it explains the reason why the effect of the time constants of the smoothing filter were similar among receiver sites for L5 frequency in Figure 2B. Since the two different sites equipped with the Trimble receiver exhibit the similar results which are different from the results of other receivers, it is unlikely to be due to an environmental reason. Rather, it is more likely because the Trimble receiver processes differently the GPS L1 signal. In conclusions, the time constant of the smoothing filter to compute the DF-innovation monitor is determined as the double of the measurement interval based on the test results. Since the Tenerife ground station has been developed as a GBAS research prototype, the statistics computed from this site will be used to compute the threshold of the CCD and the DF-innovation monitors. Accordingly, the 1-s time constant will be used in this study to smooth the DF-innovation monitor. If the

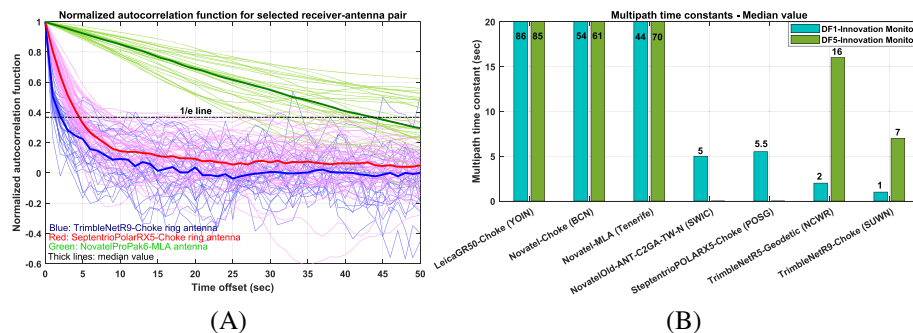


FIGURE 3 (A) The autocorrelation of the DF1-innovation monitor metric computed for SUWN (blue), POSG (red), and Tenerife (Green) sites and (B) the median value of the computed time constants of the multipath error in the DF-innovation monitor metric for L1 and L5 frequencies [Color figure can be viewed at wileyonlinelibrary.com and www.ion.org]

application is not limited to the GBAS, a slightly larger time constant, for example, the 5-s time constant, is recommended to be more robust regardless of receiver types.

3.4 | Determination of the threshold for the DF-innovation monitor

To determine the threshold, the standard deviation of the monitor must be computed. Figure 4 shows the standard deviations of the DF-innovation monitor for GPS L1/L5 and Galileo E1/E5 signals using data collection at Tenerife GBAS ground research prototype for all elevation angles. It also holds true for high elevation angles that the standard deviations are smaller for the smaller time constants of the smoothing filter. Only the standard deviation for the lowest elevation bin ranged from 5 to 10° is used to compute the threshold of the DF-innovation monitor for the conservative analysis. The computed standard deviation is further inflated using the overbound inflation factors, which are computed based on the Q-Q plot where all the actual data samples are bounded by a normal distribution with the inflated standard deviation. Figure 5 depicts the Cumulative Distribution Function (CDF) of the actual and bounded distribution. The probability in the right half plane corresponds to the values equal to (1-CDF) to observe the behavior at the tail more clearly. In the meanwhile, the

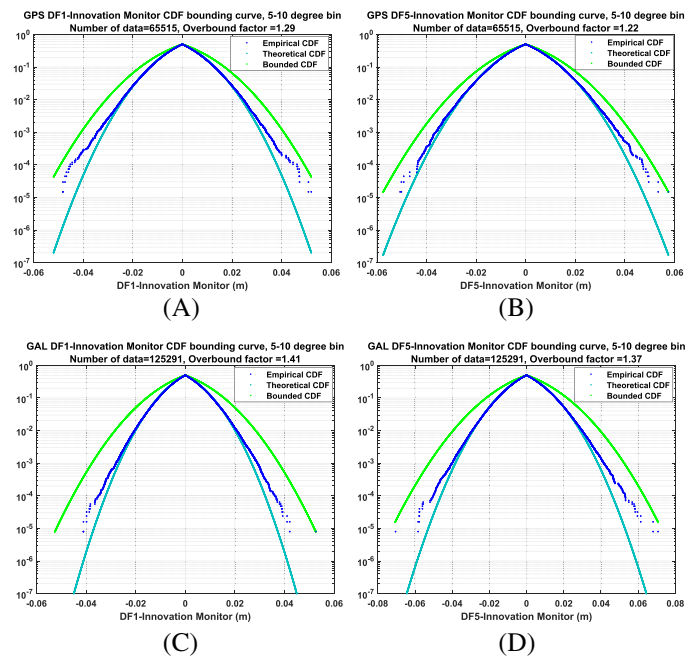


FIGURE 5 The CDF of the DF-innovation monitor for (A) GPS L1, (B) GPS L5, (C) Galileo E1, and (D) Galileo E5 [Color figure can be viewed at wileyonlinelibrary.com and www.ion.org]

threshold of the CCD monitor is also computed using the data collection at the Tenerife site. Table 2 shows the overbounded standard deviation of the CCD and the DF-innovation monitors. These standard deviations will be

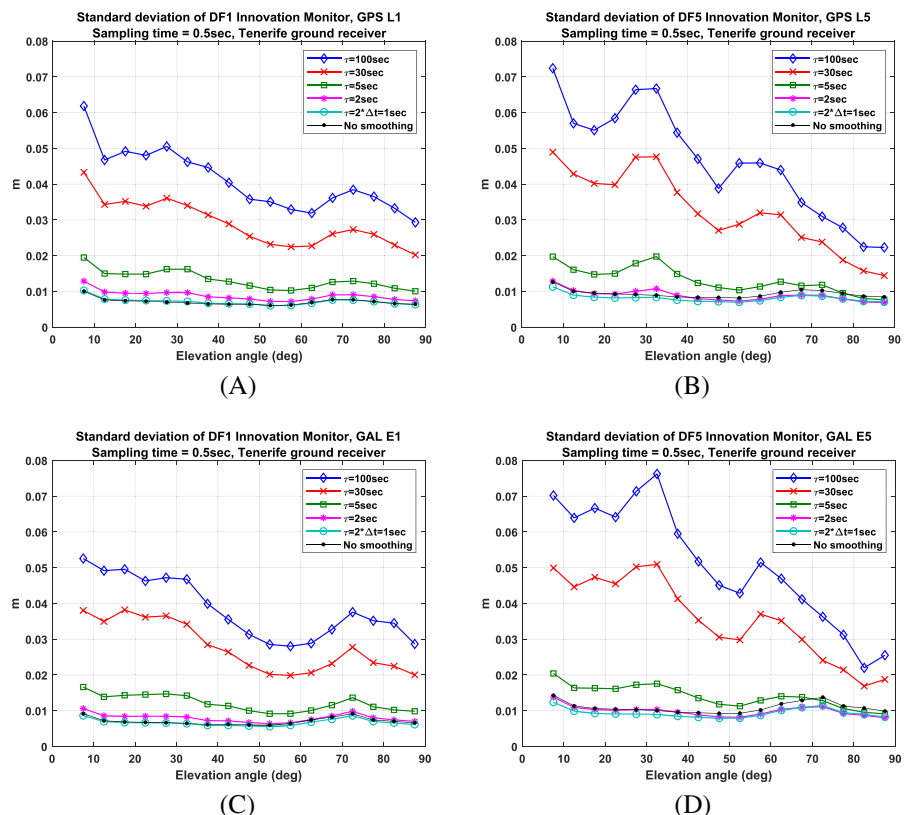


FIGURE 4 The standard deviation of the DF-innovation monitor for (A) GPS L1, (B) GPS L5, (C) Galileo E1, and (D) Galileo E5 signals at Tenerife ground receiver [Color figure can be viewed at wileyonlinelibrary.com and www.ion.org]

TABLE 2 Overbounded standard deviation of the CCD and DF-innovation monitors

	GPS		Galileo	
	DF1	DF5	DF1	DF5
CCD monitor, m/s	0.0023	0.0019	0.0039	0.0051
DF-innovation monitor, m	0.0132	0.0138	0.0121	0.0170

divided by two under the assumption that the GBAS ground station consists of four receivers.

The continuity requirement for the CCD fault is 10^{-7} per 15 s.¹⁷ The K-factor that corresponds to the associated false alarm rate has been computed in the previous research^{9,17}; this study adopts the value from the literature. For the signal deformation fault, the continuity requirement is allocated to 1.5×10^{-7} per 15 s. Since we use the Honeywell and the DF-innovation monitors to detect the signal deformation fault, half of the continuity requirement is allocated to compute the probability of false alarm for determining the threshold for each of these two monitors. Since the correlator outputs are smoothed by the moving average filter with the 30-s time constant⁷ to reduce the response time, it is assumed that there are four independent samples in the 15-s exposure time¹⁹ in a conservative manner. For the DF-innovation monitor, it is assumed that there are 15 independent samples in the exposure time for the 1-s time constant of the smoothing filter and 0.5-s measurement interval. This is the worst-case assumption in respect to evaluating missed detection probability because the larger number of the independent samples in the exposure time reduces the probability of the false alarm, thus increasing the threshold. For both cases, 15 satellites are assumed to be tracked simultaneously.

4 | MONITOR REQUIREMENTS IN GAST D STANDARDS

Previous research has shown that the requirements and methodology used for CAT I are too constraining for CAT III.⁵ For this reason, an alternative requirements methodology, which is expressed in terms of a differential range error requirement on the ground subsystem monitoring of satellite ranging faults, is used for the GAST D solution.³ This requirement is derived from the two conditions associated with the safety of landing: the first comes from the limit case²⁰ and the second is from the malfunction case.²¹ The first case requires that given the presence of a fault, the probability of unsafe landing

should not exceed 10^{-5} , and it provides the PMD requirement according to the differential range error. The second case postulates that the aircraft should be able to land safely when the probability of the fault occurrence as well as the missed detection is larger than 10^{-9} . Consequently, this condition limits the probability of exceeding 1.6 m of the differential range error to 10^{-9} , which corresponds to 10^{-5} in terms of the PMD if the *a priori* fault probability of 10^{-4} per hour is used. The derived requirement on the monitor PMD can be expressed according to the differential range error as shown in Figure 6. The PMD compliance of some specific ranging source fault monitor can be validated by verifying that for the whole threat space, the PMD of the monitor expressed as a function of the differential range error lies within the constraint region shown in Figure 6. When computing the differential range error, the latency of the correction message, which takes into account the update interval of the correction and the ground processing time, must be considered. In addition, when pairing the PMD with the differential range error, the time at which the PMD is computed needs to be determined by carefully considering the Time-To-Alert (TTA) and the latency of the integrity message, incorporating the update interval and ground processing time. The basic equation for pairing the PMD and the differential range error is shown in previous study,³ and the timing values described above will be explained in detail in the next section.

5 | SIMULATION ENVIRONMENT

The PMD compliance is tested for single- and dual-frequency modes. The PMD compliance is already verified for the GPS L1 C/A signal; however, it has not yet been completed for the modernized signals GPS L5 and

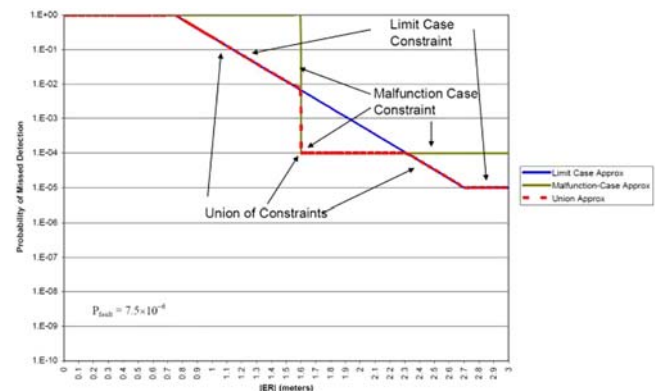


FIGURE 6 The monitor PMD requirement for the CAT II/III in standards³ [Color figure can be viewed at wileyonlinelibrary.com and www.ion.org] [Color figure can be viewed at wileyonlinelibrary.com and www.ion.org]

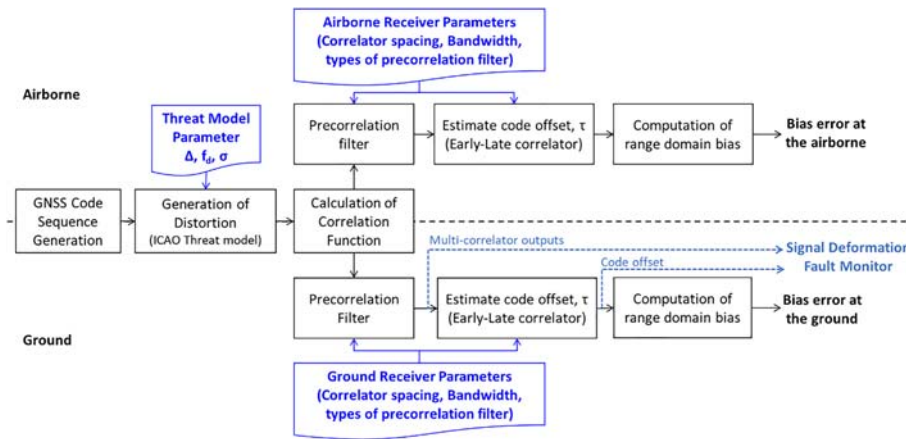


FIGURE 8 Diagram of the fault generation process [Color figure can be viewed at wileyonlinelibrary.com and www.ion.org]

the different update interval,^{16,23} the latency for the correction and integrity message are considered as separate parameters in this study.

5.2 | Fault generation process

This section describes the detailed process of the fault generation step shown in Figure 7. The overall process of the fault generation is depicted in Figure 8.

Since the signal deformation fault initially distorts the GNSS code sequence, in a first step, the GNSS code sequence is generated and the distortion on the chip level according to the ICAO threat model. Although the threat model, which is classified into digital, analog, and combined distortions, is only defined for the GPS L1 C/A signal in the standards, it is assumed that the same definition of the threats can be applied to the modernized

signal as well.¹¹ Regarding the TM parameters, the values defined in the standards are used for the GPS L1 C/A signal. For GPS L1 and Galileo E1c/E5a signals, since the parameters are not yet defined in the standards, the values proposed by Pagot¹¹ are adopted in this study. The TM is parameterized by the lead/lag of the chip (Δ), resonant frequency (f_d), and damping factor (σ).¹ The TM parameters used in this study are shown in Tables 3 and 4. The threat models stemmed from Song et al.¹⁰ for these modernized signals are currently being discussed for standardization. Here, we use $x_{\min}: \Delta x: x_{\max}$ notation to express the range of value x , where the symbols x_{\min} , x_{\max} , and Δx indicate minimum and maximum values of x and the increment of x , respectively.

In the second step, the correlation function is computed using the generated code sequence. The correlator function is input to the precorrelation filter, and after that, the code offset is estimated using the Early minus

TABLE 3 Threat model parameters for GPS L1 C/A¹

	TMA	TMB	TMC
GPS L1	$\Delta = -0.12:0.01:0.12$, chip	$\Delta = 0$, chip	$\Delta = -0.12:0.01:0.12$, chip
	$f_d = 0$, MHz	$f_d = 4:0.1:17$, MHz	$f_d = 7.3:0.1:13$, MHz
	$\sigma = 0$, Mnepers/s	$\sigma = 0.8:0.5:8.8$, Mnepers/s	$\sigma = 0.8:0.5:8.8$, Mnepers/s

TABLE 4 Threat model parameters for GPS L5 and Galileo E1c/E5a¹¹

	TMC				
	TMB				
	Area 1		Area 2		
	TMA				
	Δ , chip	f_d , MHz	σ , Mnepers/s	f_d , MHz	$\sigma/(f_d)^2$
Galileo E1c	-0.12:0.01:0.12	1:1:4	1:0.2:26	3:1:19	0.07:0.05:5
		1:1:19	0.05:0.1:1		
		4:1:19	1:1:26		
GPS L5/Galileo E5a	-0.12:0.01:0.12	3:1:19	0:4:24	4:1:19	0.06:0.075:3.5

TABLE 5 Receiver configurations for the ground and airborne

	GPS L1/Galileo E1c		GPS L5/Galileo E5a	
	Ground	Airborne	Ground	Airborne
Chip spacing, chip	0.1	0.08, 0.1, 0.12	1	0.9, 1 1.1
Precorrelation bandwidth, MHz	24	12:2:24	24	12:2:24
Precorrelation filter	(1) The sixth-order Butterworth filter	(2) The sixth-order Butterworth filter (3) 0-group delay resonator (4) 150 ns differential group delay resonator (5) 150 ns differential group delay sixth-order Butterworth	(1) The sixth-order Butterworth filter	(2) The sixth-order Butterworth filter (3) 0-group delay resonator (4) 150 ns differential group delay resonator (5) 150 ns differential group delay sixth-order Butterworth

Late (EL) correlator. For GPS L1 C/A, BPSK(1) is used as a local replica and BPSK(10) is used for GPS L1 and Galileo E5a signals. For Galileo E1c, BOC(1,1) is used as a local replica. The impact of the fault varies according to the receiver configurations of precorrelation filter, bandwidth, and correlator chip spacings. Therefore, the receiver configurations at the ground and the airborne are input to the fault generation program to take into account the impact of the different receiver settings. The receiver settings used in this study are shown in Table 5 according to the ICAO standards for GPS L1 C/A^{1,11} and the draft of the SBAS multifrequency and multi-constellation standards¹² for the other signals. Finally, the code offset estimated from the faulted code sequence is compared with the nominal value, and then the difference between those two values in the chip domain is transformed to the range domain using the chip period, chipping rate, and the speed of light. The resultant range domain errors at the ground and the airborne correspond to e_{ground} and e_{air} before the smoothing filter is applied in Figure 7. This fault generation process has been validated by Pagot and Julien et al.^{11,24}

5.3 | Test configuration

The values used for the message latencies from the ground and the TTA allocated to the ground are shown in Table 6. In the GAST D solution, because the corrections and integrity information are broadcasted in the same message, the latency of the correction and the integrity message is set to the same value of 1.5 s, taking into account the 0.5-s update interval and the 1 s of ground delay.³ In GAST F, the latency of the correction is set to 3 s in this test, allowing 2 s of update interval and 1 s of ground delay to accommodate the increased correction

TABLE 6 Simulation configuration

Simulation Parameters, s	GAST D	GAST F
Latency of correction message (τ_G)	1.5	3
Latency of Integrity message (τ_I)	1.5	
TTDABA	1.5	
Time constant for carrier smoothing	30	100
Time constant for smoothing monitor metrics	Honeywell monitor CCD monitor DF-innovation monitor	30 30 -
Time of fault onset (t_f)	180	
Filter initialization time at ground (t_g)	0	
Filter initialization time at airborne (t_a)		Postconvergence case: 50 Transient case: 180

messages due to the multiconstellation with the limited bandwidth of the VHF Data Broadcast (VDB). Unlike the correction message, the update interval of the integrity message must remain unchanged to cope with the same TTA requirement. Thus, the integrity message should be broadcasted separately from the correction message.^{16,23} Regarding the carrier smoothing filter, a 30-s time constant is used for the GAST D solution. For GAST F, it is under discussion to use a 100-s time constant in order to leverage the existing 100-s corrections provided in GBAS Message Type 1 (MT1). The time constants for smoothing monitor metrics are also given in Table 6.

In the simulation scenario, the fault is set to occur at 180 s, and the initialization time of the carrier smoothing filter at the ground is set to 0 s. For the airborne side, we

considered the two cases for the filter initialization time: One is the case when the airborne filter is initialized before the fault onset, and the other represents the case when the filter is initialized at or right after the fault onset. This is to take into account the possibility of having different differential range errors according to the airborne filter initialization times even under identical receiver configurations. The two cases are shown in Figures 9 and 10, respectively.

In Figure 9, the differential range error gradually increases over time, since the filters are initialized earlier

than the fault onset time both at the ground and aircraft. It can be clearly observed that the response time of the differential range error depends on the time constant. It should be noted that the smoothing filter used for the ground monitor is separate from that for the ranging measurements. Using the time history of the differential range error and the PMD of the ground monitor, the PMD compliance can be validated with respect to the requirement as shown in Figure 9C. For the post-convergence case, the PMD compliance results for two cases of time constants are anticipated: one with the

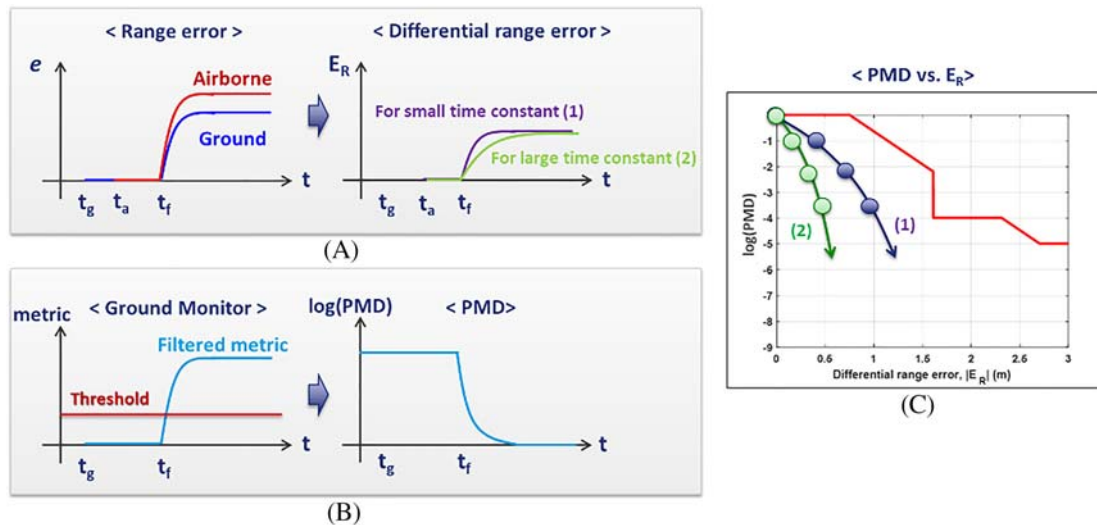


FIGURE 9 Description of post-convergence case and the effect of time constant of carrier smoothing for the PMD compliance: (A) Range errors at ground and airborne and associated differential range error, (B) ground monitor and corresponding PMD, and (C) the PMD compliance curve for small and large time constants of the smoothing filter (red line: the PMD requirement) [Color figure can be viewed at wileyonlinelibrary.com and www.ion.org]

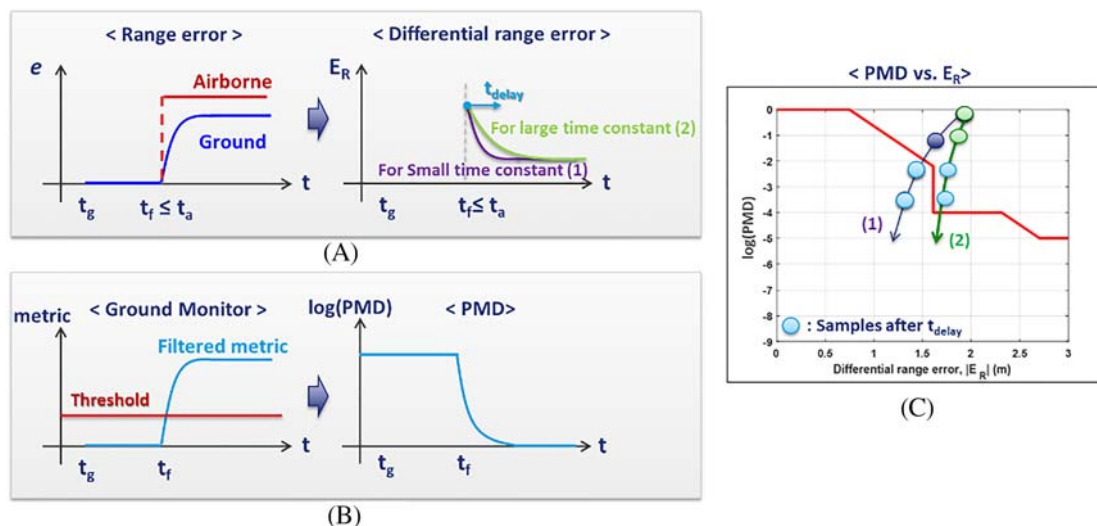


FIGURE 10 Description of transient case and the effect of time constant of carrier smoothing for the PMD compliance: (A) Range errors at ground and airborne and associated differential range error, (B) ground monitor and corresponding PMD, and (C) the PMD compliance curve for small and large time constants of the smoothing filter with t_{delay} (red line: the PMD requirement) [Color figure can be viewed at wileyonlinelibrary.com and www.ion.org]

small time constant, denoted as 1, and the other with the large time constant, denoted as 2 in Figure 9A,C. It can be anticipated that using a larger time constant is more beneficial in terms of the PMD compliance for the post-convergence case.

However, the differential range error gradually decreases with time for the transient case as shown in Figure 10A. This is due to the output of the airborne filter instantly converging to the steady-state value. The ground monitor acts in the same manner as in the post-convergence case. In this respect, it is beneficial to use a smaller time constant for the carrier smoothing of the range as shown in Figure 10C. However, in the transient-case, there is a strong possibility that the requirement is not satisfied immediately after the fault onset, because the differential range error is large at that moment. Therefore, the time delay, denoted as t_{delay} , is generally introduced to avoid these cases of PMD noncompliance.^{5,9} The t_{delay} indicates the waiting time at the airborne from the filter initialization time to the time when the airborne incorporates the correction and its measurement for computing the position. In Figure 10C, it is observed that the PMD versus the differential range curve falls within the PMD constraints when only the data samples after the t_{delay} are considered. It should be noted that the t_{delay} needs to be increased for the PMD compliance if the time constant of the carrier smoothing is increased. In conclusion, the preferable time constant of the carrier smoothing is different for the post-convergence and transient cases.

It should be noted that the introduction of the time delay is only useful for the Honeywell and CCD monitors. The DF-innovation monitor is often able to capture the impact of the fault as soon as the fault occurs. Therefore, the faults that cannot be detected by the DF-innovation monitor at the time of fault onset should be detected by Honeywell and the CCD monitors. The time history of each monitor for the TM C1 (TM C, Area

1 defined in Table 4) type fault with $\Delta = -0.1$ chip, $f_d = 1$ MHz, and $\sigma = 23.8$ Mnepers/s for the Galileo E1c signal with its threshold is shown in Figure 11.

6 | TEST RESULTS

6.1 | Single-frequency test mode (GAST D)

Table 7 shows the overall results of the PMD compliance for the single-frequency mode. Since the GAST D solution supports CAT II/III operations as defined in the standards for GPS L1 C/A, the assessment process is straightforward. In order to compare the monitoring performance for the GPS L1 signal with the other modernized signals, the test condition is slightly modified for GPS L5 and Galileo E1c/E5a signals. That is, as the multifrequency and multiconstellation concepts are adopted in the GAST F solution, the latency of correction messages, which is used for the assessment for the modernized signal, is set to the value recommended for the GAST F solutions even when the processing mode is single-frequency.¹⁶ In addition, to investigate the effect of the time constant of the carrier smoothing for the pseudorange, 30 and 100 s of the time constants were tested for the modernized signals. Here, the t_{delay} is set to 50 s.⁹

As a result, the existing signal deformation fault monitors readily protect the airborne users from the any type of fault for GPS L1 C/A signal regardless of receiver configurations. However, there are some noncompliant cases for other signals. For Galileo E1c, if the 30-s time constant is used, the monitors fail to protect the airborne user against the TMB and TMC in the post-convergence case. If the time constant is increased to 100 s, the transient case becomes problematic for all fault types. The GPS L1 C/A and Galileo E1c have different modulations; thus, the Honeywell monitor showed a different

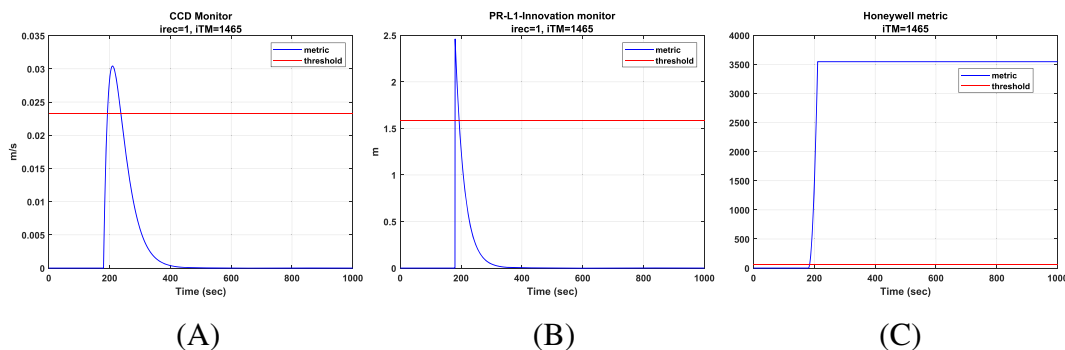



FIGURE 11 Time history of (A) the CCD monitor, (B) the DF1-innovation monitor, and (C) Honeywell monitor for the TM C1 type fault ($\Delta = -0.1$ chip, $f_d = 1$ MHz, and $\sigma = 23.8$ Mnepers/s), Galileo E1c signal. The red line indicates the threshold [Color figure can be viewed at wileyonlinelibrary.com and www.ion.org]

TABLE 7 The PMD compliance result for single-frequency mode test (GAST D) [Color table can be viewed at wileyonlinelibrary.com and www.ion.org]

		PMD Compliance Results				
		GPS L1		Galileo E1c		GPS L5/Galileo E5a
Time Constant for Carrier Smoothing		30 s	30 s	100 s	30 s	100 s
TMA	Post-convergence					
	Transient					
TMB	Post-convergence					
	Transient					
TMC	Post-convergence					
	Transient					
Note		TTDABA = 1.5 s, $\tau_G = 1.5$ s, $\tau_I = 1.5$ s			TTDABA = 1.5 s, $\tau_G = 3.0$ s, $\tau_I = 1.5$ s	
Legend		Green: Compliance				
		Red: Non-compliance				

performance for these two signals. For GPS L5 and Galileo E5a signals, the PMD is compliant for all threat models and receiver configurations when the time constant is set to 30 s; however, the transient case becomes problematic if the time constant increases to 100 s. Based on these observations, it verifies the argument in the previous section that the larger time constant of the carrier smoothing filter is preferable for the post-convergence case; however, it is more beneficial to use smaller time constants for the transient case, as demonstrated in Figures 9 and 10.

Figures 12 and 13 depict the PMD noncompliant regions in the TMC1 (TMC Area 1) and TMC2 (TMC Area 2) threat space for Galileo E1c and Galileo E5a. The PMD noncompliance observed for the post-convergence case, shown in Figure 12A, occurs for small values of resonant frequency, f_d and damping factor, σ . It is not presented in the figure, but there were four PMD noncompliant cases for the TM C2 (TMC Area 2 defined in Table 4)-type faults, which correspond to $(\Delta, f_d, \sigma) = (-0.08, 15, 927)$, $(-0.07, 17, 887.23)$, and $(-0.06, 19, 729.22)$ for airborne receiver configuration with (chip

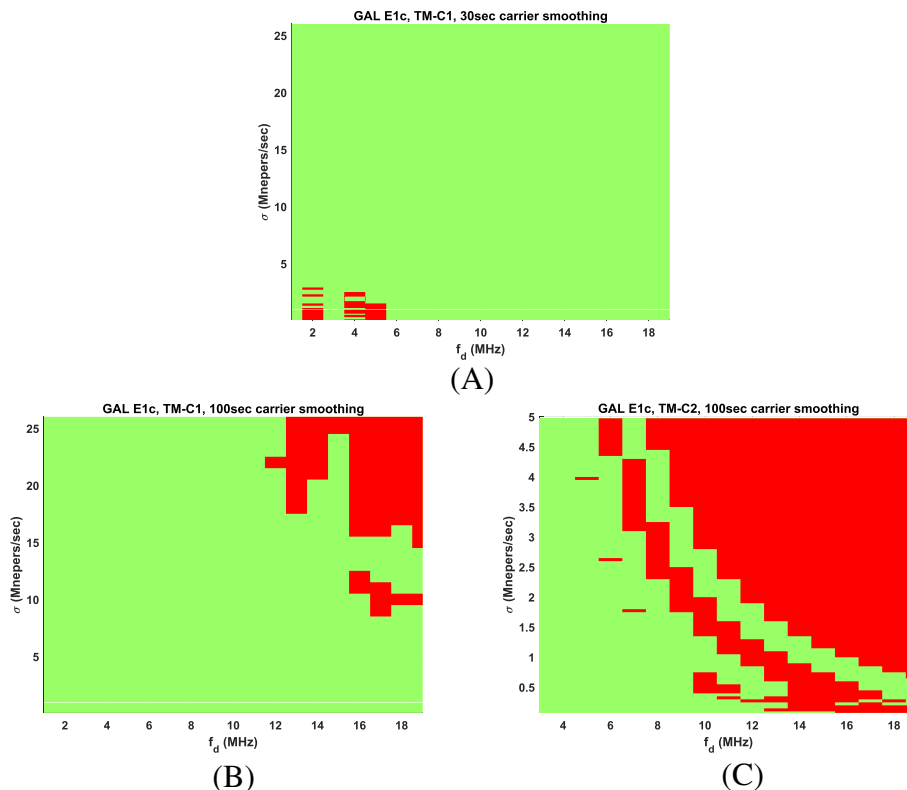
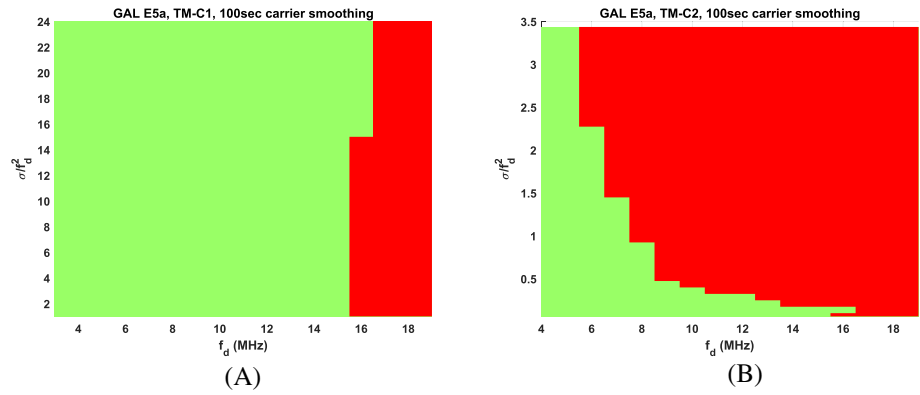


FIGURE 12 Noncompliant region in the threat space for Galileo E1c: (A) TMC1, 30-s time constant, (B) TMC1, 100-s time constant, and (C) TMC2, 100-s time constant [Color figure can be viewed at wileyonlinelibrary.com and www.ion.org]

FIGURE 13 Noncompliant region in the threat space for Galileo E5a: (A) TMC1, 100-s time constant, and (B) TMC2, 100-s time constant [Color figure can be viewed at wileyonlinelibrary.com and www.ion.org]



spacing, precorrelation filter, bandwidth) = (0.08, 4, 12), and $(\Delta, f_d, \sigma) = (-0.06, 19, 729.22)$ for airborne receiver configuration with (chip spacing, precorrelation filter, bandwidth) = (0.08, 4, 14). Whereas, noncompliance for the transient case usually takes place for the larger values of resonant frequency and damping factor, as shown in Figures 12B,C and 13. These conditions correspond to the situation when the steady-state tracking error at the ground and the impact of the distortion on the correlator outputs, as are measured by the Honeywell monitor, are not significant. However, at the same time, the steady-state tracking error at the airborne is much larger than that of the ground receiver.

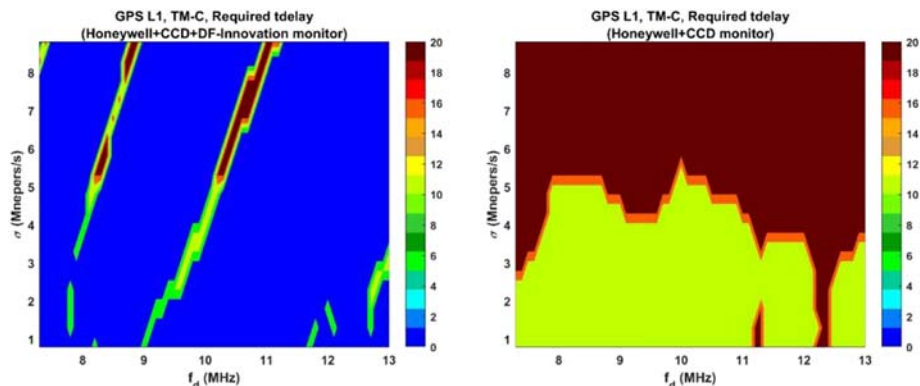
6.2 | Dual-frequency test mode (GAST F)

In this section, the PMD compliance is assessed for the dual-frequency processing mode. For the GPS L1/L5 processing, a single fault on L1 and L5 frequencies is considered separately, and the same is true for the Galileo E1/E5 processing. The airborne navigation mode is assumed to be based on the IF pseudorange combination, which is defined as the following equation.

$$\rho_{IF} \equiv \frac{\gamma}{\gamma-1} \rho_1 - \frac{1}{\gamma-1} \rho_5 = 2.26\rho_1 - 1.26\rho_5. \quad (9)$$

As seen from Equation (9), the differential range error caused by a fault on L1 and L5 frequencies will be increased by factors of 2.26 and 1.26, respectively, compared with those in the single-frequency mode. The increase of the differential range error may jeopardize the PMD compliance of the monitor recalling the PMD requirement plot in Figure 6. In spite of this, since the performance of the monitor based on the dual-frequency measurement has improved significantly thanks to the elimination of the ionospheric delay, it will mitigate this increase. The PMD compliance is assessed under two test conditions: first, the case when the Honeywell and the DF CCD monitors are used, and second, with the addition of the DF-innovation monitor. For both cases, the PMD was compliant for all types of fault and receiver configurations when the t_{delay} is set to 50 s. To understand the benefit of using the DF-innovation monitor, the required t_{delay} for the PMD compliance was investigated for the TMC-type faults for all signals. The values of t_{delay} ranging from 0 to 160 s at intervals of 10 s were tested. The required t_{delay} is plotted over the threat space represented by the resonant frequency and the damping factor. To be more specific, the t_{delay} plotted for each location of the threat space indicates the required time delay at the airborne for the monitors to be compliant for all values of Δ and receiver configurations. From the area with the dark blue in the left plots in Figures 14, 15, and 16, it can

FIGURE 14 Required t_{delay} for the PMD compliance for the TMC under GPS L1 fault mode (left: with DF-innovation monitor, right: without proposed monitor) [Color figure can be viewed at wileyonlinelibrary.com and www.ion.org]



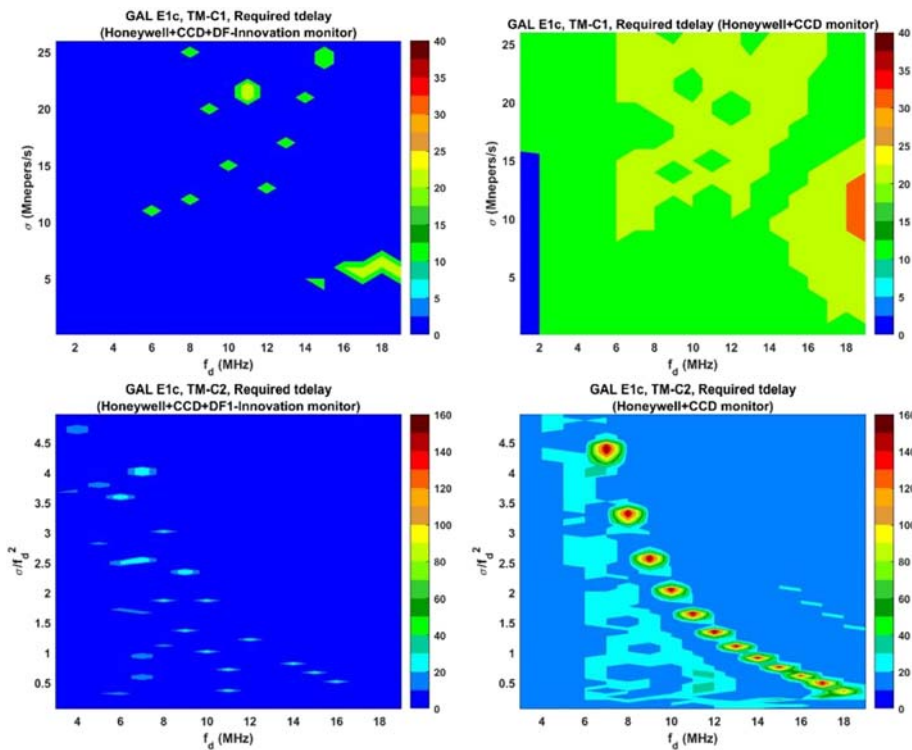


FIGURE 15 Required t_{delay} for the PMD compliance for the TMC1 under Galileo E1c fault mode in the upper panel and TMC2 in the lower panel (left column: with the DF-innovation monitor, right column: without the proposed monitor) [Color figure can be viewed at wileyonlinelibrary.com and www.ion.org]

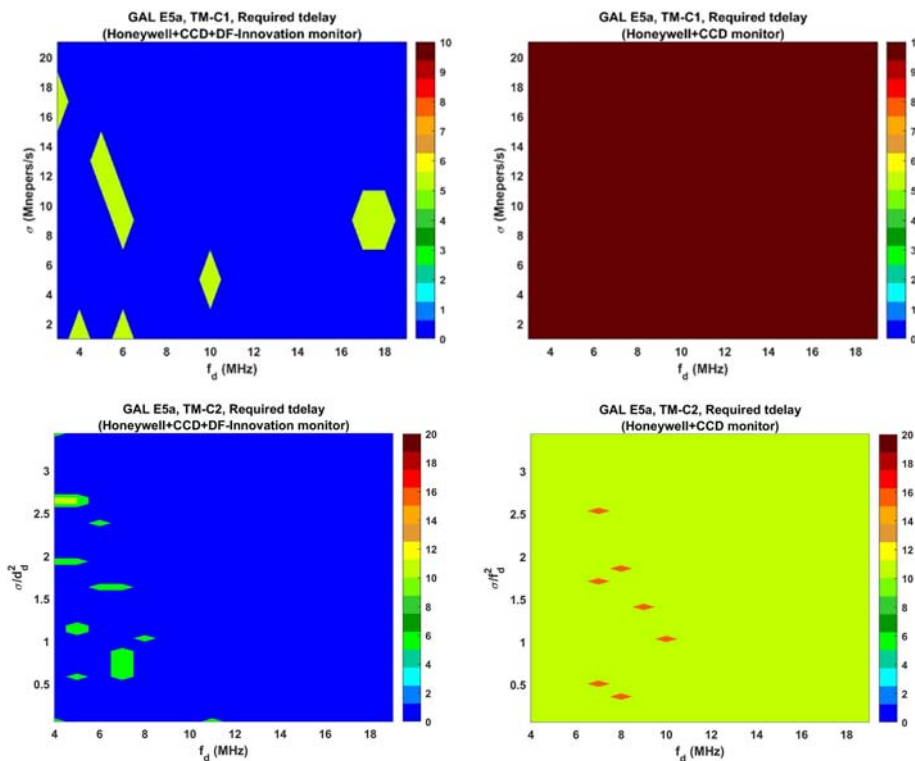


FIGURE 16 Required t_{delay} for the PMD compliance for the TMC1 under Galileo E5a fault mode in the upper panel and TMC2 in the lower panel (left column: with the DF-innovation monitor, right column: without the proposed monitor) [Color figure can be viewed at wileyonlinelibrary.com and www.ion.org]

be observed that the solution becomes compliant instantly over most of the threat space thanks to the DF-innovation monitor. The region of the threat space, which is not instantly compliant as soon as fault occurs, is protected by the Honeywell and the CCD monitors with some nonzero t_{delay} . If the DF-innovation monitor is not used, then large values of t_{delay} are required for PMD

compliance as seen in the right plots in Figures 14, 15, and 16. The large values of t_{delay} indicate that the airborne receiver must wait additional time following filter initialization before incorporating the corrected measurements.

Table 8 shows the required t_{delay} for the monitors to be compliant for all signals, fault cases, and receiver

TABLE 8 Required t_{delay} for the PMD compliance with and without using the DF-innovation monitor

	Required t_{delay} , s				
	GPS L1	GAL E1c	GPS L5	GAL E5a	Overall
Honeywell SQM + ENAC CCD	30	160	20	20	160
Honeywell SQM + ENAC CCD + DF-innovation monitor	30	30	20	20	30

configurations. For GPS L1, GPS L5, and Galileo E5a signals, the required t_{delay} was the same for both simulation conditions with and without using the DF-innovation monitor even if the number of cases that require large values of t_{delay} are much smaller for the simulation condition with the DF-innovation monitor. For Galileo E1c signal, the required value of t_{delay} reaches 160 s when the DF-innovation monitor is not used. However, using the DF-innovation monitor can significantly reduce the required t_{delay} to 30 s. Moreover, the recommended t_{delay} can be further reduced to 30 s, which is below the recommended t_{delay} of 50 s, and thus avoid the unnecessary delays for the use of newly available satellites.

7 | CONCLUSIONS

This paper proposes the DF-innovation monitor which can improve the detection performance right after the fault onset where the existing Honeywell and ENAC DF-CCD monitors are vulnerable due to the response time associated with the smoothing filter for the metrics. Consequently, the proposed monitor is effective in reducing the required time delay, which is the waiting time at the airborne receiver before corrected measurements may be incorporated into the positioning solution. Based on the analysis of the error components in the proposed monitor metrics, according to the time constants of the smoothing filter, a 1-s time constant is determined as optimal for the new monitor. In addition, the performance of the signal deformation monitors has been assessed for GAST D and GAST F with respect to the PMD requirement as defined in the standards. The PMD requirement for the GAST F may be relaxed in the future due to the potential use of multiple constellations under a Dual-Frequency and Multi-Constellation (DFMC) GBAS concept. However, the same requirement as the GAST D is used for the GAST F in this conservative analysis. The latency of correction and integrity messages, the TTDABA, and the time constant of the carrier smoothing filter for the range are taken into account according to the standards³ and the recent agreement on GAST F within the SESAR studies¹⁶ and previous research. The threat space for the GPS

L1 C/A signal is taken from the ICAO standard¹ and those for the modernized signals are adopted from previous work at ENAC.¹¹

For the single-frequency mode, compliance is achieved for the GPS L1 C/A signal, regardless of the types of faults and receiver configurations. For the Galileo E1c signal, the two values of the time constant for the carrier smoothing filter are tested. When the 30-s time constant is used, the post-convergence under the TMB and TMC-type faults becomes problematic. However, the transient-case under all types of fault becomes non-compliant when the time constant is increased to 100 s. For GPS L5 and Galileo E5a signals, compliance is achieved for all types of faults and receiver configuration when the 30-s time constant is used. However, for the 100-s time constant, the transient case becomes problematic for all types of fault. It confirms that the smaller time constant is beneficial for the post-convergence case and the larger time constant is preferable for the transient case. These findings can be considered when recommending the time constant of the pseudorange smoothing filter for GAST F standardization.

For the dual-frequency mode, two monitor combinations were tested: one using the existing Honeywell and ENAC DF-CCD monitors and the other with the addition of the DF-innovation monitor. Under both scenarios the airborne users are protected from any type of signal deformation fault and for all receiver configurations. However, using only the Honeywell and ENAC DF-CCD monitors requires 160 s of time delay at the aircraft for PMD compliance to be achieved for all signals, threat models, and receiver configurations. However, if the proposed DF-innovation monitor is also used, the time delay can be significantly reduced to 30 s.

In this study, the minimum value of the PMD of all monitors is used to assess the PMD compliance. For a more accurate assessment, the joint PMD may be evaluated. Therefore, the correlation among monitors will be investigated and considered for computing the PMD as a future work. Furthermore, the evaluation of monitoring performance over an extended threat space for Galileo signals may be required following standardization.

ACKNOWLEDGEMENTS

This work is funded by the European Union, Eurocontrol, and industry partners under the Horizon 2020 program, specifically within the frame of SESAR 2020 PJ14-03-01. The authors would like to thank INDRA Navia, INDRA Satnav, and ENAIRE for the use of their data collections.

ORCID

Carl Milner  <https://orcid.org/0000-0003-3614-1510>

REFERENCES

1. ICAO Annex 10 to the Convention on International Civil Aviation, Vol. 1, Amendments 90; 2006.
2. ICAO Annex 10 to the Convention on International Civil Aviation, Vol. 1, Amendments 91; 2018.
3. ICAO SARPs. GBAS CAT II/III development baseline SARPs and conceptual framework for the proposal for GBAS to support CAT III operations. NSP WGW November 2009 Report. https://www.icao.int/safety/airnavigation/documents/gnss_cat_ii_iii.pdf.
4. Shloss P, Phelts RE, Walter T, Enge P. A simple method of signal quality monitoring for WAAS LNAV/VNAV. *Proceedings of the 15th International Technical Meeting of the Satellite Division of The Institute of Navigation (ION GPS 2002)*. Portland, OR; September 2002, pp. 800–808.
5. Brenner M, Liu F. Ranging source fault detection performance for category III GBAS. *23rd International Technical Meeting of the Satellite Division of The Institute of Navigation*. Portland, OR; September 21–24, 2010, pp. 2618–2632.
6. Daly P, Riley S, Raby P. Recent advances in the implementation of GNSS. *Proceedings of the 6th International Technical Meeting of the Satellite Division of The Institute of Navigation (ION GPS 1993)*. Salt Lake City, UT; September 1993, pp. 433–440.
7. Phelts RE. Multicorrelator techniques for robust mitigation of threats to GPS signal quality. Ph.D. Thesis. Department of Mechanical Engineering and the Committee on Graduate Studies, Stanford University, Stanford, CA; 2001.
8. Liu F, Brenner M, Tang CY. Signal deformation monitoring scheme implemented in a prototype local area augmentation system ground installation. *Proceedings of the 19th International Technical Meeting of the Satellite Division of The Institute of Navigation (ION GNSS 2006)*. Fort Worth, TX; September 2006, pp. 367–380.
9. Jiang Y, Milner C, Macabiau C. Code carrier divergence monitoring for dual-frequency GBAS. *GPS Sol*. 2017;21(2):769–781.
10. Song J, Milner C, Selmi I, Bouterfas S, Julien O. Assessment of dual-frequency signal quality monitor to support CAT II/III GBAS. *Proceedings of the 32nd International Technical Meeting of the Satellite Division of The Institute of Navigation (ION GNSS + 2019)*. Miami, FL; September 2019, pp. 508–518.
11. Pagot J-B. Modeling and monitoring of new GNSS signal distortions in the context of civil aviation. PhD Dissertation. Ecole Nationale de l'Aviation Civile, France; 2016.
12. Baseline development standards for the validation of draft Annex 10, Volume I amendments relating to dual-frequency, multi-constellation(DFMC) SBAS, Appendix A to the Report on Agenda Item 2. 5th Meeting of the Navigation Systems Panel (NSP/5); 2018.
13. Shively CA. Derivation of acceptable error limits for satellite signal faults in LAAS. *Proceedings of the 1999 12th International Technical Meeting of the Satellite Division of the Institute of Navigation (ION GPS 1999)*. Nashville, TN; September 1999, pp. 761–770.
14. Zaugg T. A new evaluation of maximum allowable errors and missed detection probabilities for LAAS ranging source monitors. *Proceedings of the 58th Annual Meeting of The Institute of Navigation and CIGTF 21st Guidance Test Symposium*. Albuquerque, NM; June 2002, pp. 187–194.
15. Rife J, Phelts RE. Formulation of a time-varying maximum allowable error for ground-based augmentation systems. *IEEE Trans Aero Electron Syst*. 2008;44(2):548–560.
16. SESAR. D3.7.1 monitoring, integrity and performance, 03.00.00, November 2015.
17. Simili DV, Pervan B. Code-carrier divergence monitoring for the GPS local area augmentation system. *Proceedings of IEEE/ION PLANS 2006*. San Diego, CA; April 2006, pp. 483–493.
18. Hwang PY, McGraw GA, Bader JR. Enhanced differential GPS carrier-smoothed code processing using dual-frequency measurements. *Navigation*. 1999;46:127–138.
19. Pervan B, Khanafseh S, Patel J. Test statistic auto- and cross-correlation effects on monitor false alert and missed detection probabilities. *Proceedings of the 2017 International Technical Meeting of The Institute of Navigation*. Monterey, CA; January 2017, pp. 562–590.
20. EASA, CS AWO 1. Joint aviation requirements—all weather operations, Subpart 1: Automatic Landing Systems. EASA Report. February 2018. <https://www.easa.europa.eu/sites/default/files/dfu/Easy%20Access%20Rules%20for%20CS-AWO.pdf>.
21. FAA Advisory Circular 120-28D. Criteria for approval of category III weather minima for takeoff, landing and rollout. July 13, 1999.
22. Minimum operational performance standards (MOPS) for GPS local area augmentation system airborne equipment, RTCA DO-253C. Washington, DC; 2008.
23. Milner C, Guilbert A, Macabiau C. Evolution of corrections processing for the MC/MF ground based augmentation system (GBAS). *Proceedings of the 2015 International Technical Meeting of The Institute of Navigation*. Dana Point, CA; January 2015, pp. 364–373.
24. Julien O, Selmi I, Pagot J-B, Samson J, Fernandez FA. Extension of EWF threat model and associated SQM. *Proceedings of the 2017 International Technical Meeting of The Institute of Navigation*. Monterey, CA; January 2017, pp. 492–507.

How to cite this article: Song J, Milner C, Selmi I. Signal deformation fault monitors for dual-frequency GBAS. *NAVIGATION-US*. 2020;67: 379–396. <https://doi.org/10.1002/navi.360>